Original Article

Multi-stimuli-responsive chitosan-functionalized magnetite/poly(ε-capro-lactone) nanoparticles as theranostic platforms for combined tumor magnetic resonance imaging and chemotherapy

Gracia García-García, PhD[a], Carlos Caro, PhD[b], Fátima Fernández-Álvarez, PhD[c],
María Luisa García-Martín, PhD[b,d], José L. Arias, PhD[c,e,f],*

[a]*Faculty of Experimental Sciences, Universidad Francisco de Vitoria, Ctra. Pozuelo-Majadahonda Km 1,800, 28223 Pozuelo de Alarcón, Madrid, Spain*
[b]*Andalusian Centre for Nanomedicine and Biotechnology (BIONAND), Junta de Andalucía–Universidad de Málaga, C/ Severo Ochoa, 35, 29590 Málaga, Spain*
[c]*Department of Pharmacy and Pharmaceutical Technology, Faculty of Pharmacy, University of Granada, 18071 Granada, Spain*
[d]*Biomedical Research Networking Center in Bioengineering, Biomaterials and Nanomedicine (CIBER-BBN), Málaga, Spain*
[e]*Institute of Biopathology and Regenerative Medicine (IBIMER), Center of Biomedical Research (CIBM), University of Granada, Av. del Conocimiento, 18016 Granada, Spain*
[f]*Biosanitary Research Institute of Granada (ibs.GRANADA), University of Granada, Av. de Madrid, 15, 18012 Granada, Spain*

Revised 2 June 2023

Abstract

Chitosan-functionalized magnetite/poly(ε-caprolactone) nanoparticles were formulated by interfacial polymer disposition plus coacervation, and loaded with gemcitabine. That (core/shell)/shell nanostructure was confirmed by electron microscopy, elemental analysis, electrophoretic, and Fourier transform infrared characterizations. A short-term stability study proved the protection against particle aggregation provided by the chitosan shell. Superparamagnetic properties of the nanoparticles were characterized *in vitro*, while the definition of the longitudinal and transverse relaxivities was an initial indication of their capacity as T_2 contrast agents. Safety of the particles was demonstrated *in vitro* on HFF-1 human fibroblasts, and *ex vivo* on SCID mice. The nanoparticles demonstrated *in vitro* pH- and heat-responsive gemcitabine release capabilities. *In vivo* magnetic resonance imaging studies and Prussian blue visualization of iron deposits in tissue samples defined the improvement in nanoparticle targeting into the tumor when using a magnetic field. This tri-stimuli (magnetite/poly(ε-caprolactone))/chitosan nanostructure could find theranostic applications (biomedical imaging & chemotherapy) against tumors.
© 2023 The Author(s). Published by Elsevier Inc. This is an open access article under the CC BY-NC-ND license (http://creativecommons.org/licenses/by-nc-nd/4.0/).

Keywords: Chitosan; Dual pH- and heat-triggered drug release; Magnetic resonance imaging; Magnetite; Poly(ε-caprolactone)

Background

Single or combined chemotherapies using gemcitabine (GEM) can make possible satisfactory tumor response rates in numerous malignancies: pancreatic,[1] lung,[2] breast,[3] ovarian,[4] or bladder[5] cancers, to cite just some representative examples. However, limited success of this chemotherapeutic is principally associated to tumor heterogeneity, development of metastases and/or multidrug resistances, systemic toxicity, and the generation of subtherapeutic levels at the tumor site.[6] In addition, late diagnosis is an additional reason largely contributing to the progress of the disease.[7]

Formulation of multifunctional nanoparticles (NPs) is making possible improved cancer diagnosis, even at early stages,[8] better antitumor strategies based on chemotherapy,[9] gene therapy,[10] phototherapy,[11] and/or hyperthermia,[12] and the growth of cancer theranosis.[13] These hybrid nanostructures combine inorganic materials, *e.g.* iron oxides, with organic components, principally polymers[14] and lipid-based systems.[15] These nanoparticulate systems have been described to maximize the accumulation of diagnostic and/or therapeutic agents into the tumor interstitium or cell, and to overcome cancer drug resistances, while minimizing the *in vivo* distribution to non-targeted sites and the rapid body clearance.[16]

Superparamagnetic iron oxides, *i.e.* magnetite (Fe_3O_4) or maghemite (γ-Fe_2O_3), are habitual components of the structure of cancer theranostics, given that they provide magnetic hyperthermia, magnetic drug targeting, and magnetic resonance imaging (MRI) contrast functionalities.[17] Embedding these magnetic nuclei into a polymeric matrix, *e.g.* poly(D,L-lactide-*co*-glycolide) or PLGA,[18] poly(ε-caprolactone) or PCL,[14] and chitosan or CS,[19] has made possible the formulations of NPs joining cancer diagnosis and therapeutic functionalities.[20] Furthermore, biocompatibility, biodegradability, and low toxicity of these nanostructures have been demonstrated.[21]

PCL offers appropriate properties for the delivery of chemotherapeutic agents, *e.g.*, adequate loading values and sustained or biphasic release profiles.[22] PCL matrices further exhibit dual stimuli-triggered drug release profiles in response to pH and temperature changes. Concretely, rapid release of drug molecules at the characteristic acidic environment of tumors is the consequence of the accelerated hydrolysis of the ester linkages in the polymer architecture.[14,23] On the contrary, drug release triggered by temperature has been associated to heat-induced ageing and degradation of the polymer matrix.[24,25] The latter behavior is of interest when including superparamagnetic particles into PCL NPs: heat generated by these iron oxides under exposure to an alternating magnetic field, the so-called magnetic hyperthermia effect, may favor PCL degradation, thus activating drug release.[26]

CS is a promising alternative to polyethylene glycol in the formulation of long-circulating NPs. The positively-charged and hydrophilic stealth CS shell onto the particle minimizes opsonization, thus prolonging NP blood circulation.[27,28] Additionally, this shell facilitates the uptake by targeted cells,[29,30] and provides tumor pH-triggered drug release capabilities, given their solubility at acidic pHs.[31,32]

Here, it is described a reproducible methodology to prepare CS-functionalized Fe_3O_4/PCL or (Fe_3O_4/PCL)/CS particles. This nanostructure was characterized by dynamic light scattering (DLS), scanning transmission electron microscopies, elemental analysis, Fourier transform infrared (FTIR) spectroscopy, and inductively coupled plasma-high resolution mass spectrometry (ICP-HRMS). Magnetic responsiveness and short-term stability were evaluated. Toxicity evaluation of the (core/shell)/shell NPs was based on 3-(4,5-dimethylthiazol-2-yl)-3,5-diphenyl tetrazolium bromide (MTT) proliferation assays and cell morphology studies in HFF-1 human foreskin fibroblasts, and on *ex vivo* hematoxylin and eosin (H&E) histology. GEM vehiculization abilities were investigated, firstly exploring the capacity of the NPs for drug loading, and then analyzing the potential use of the particles for pH- and heat (hyperthermia)-triggered GEM release. Lastly, the possibility of using the NPs as MRI contrast agents was investigated *in vitro* by determining their longitudinal (r_1) and transverse (r_2) relaxivities, and *in vivo* by MRI. Assessment of NP biodistribution and the possibility of controlling it by using magnetic fields was done by MRI, and by Prussian blue (PB) staining. To the best of our knowledge, this is the first time that these (Fe_3O_4/PCL)/CS particles are engineered for antitumor theranostics (biomedical imaging & chemotherapy).

Materials and methods

Materials

Iron(III) chloride hexahydrate ($FeCl_3\cdot6H_2O$), iron(II) chloride tetrahydrate ($FeCl_2\cdot4H_2O$), KNO_3, $HClO_4$, HCl, EtOH, and CH_3COOH from VWR International, LLC (Spain). PCL ($M_w \approx 14$ kDa), CS (≈ 50 to 190 kDa, 75–85 % deacetylated), MTT, 4′,6-diamidino-2-phenylindole dihydrochloride (DAPI), xylene, phosphate buffered saline (PBS), calcein acetoxymethyl ester (calcein AM), potassium ferrocyanide, dichloromethane (DCM), NaOH, and GEM hydrochloride were obtained from Merck KGaA (Germany). Kolliphor® P-188 from BASF (Germany). TO-PRO®-3 iodide and dimethyl sulfoxide from ACROS Organics™ (Belgium). Dulbecco's Modified Eagle medium (DMEM), fetal bovine serum (FBS), 2 mM L-glutamine, Gibco™ penicillin-streptomycin solution (100 IU/mL), citric acid, and Triton® X-100 from ThermoFisher Scientific Inc. (USA). NH_3 from Panreac (Spain). Na_2HPO_4 and Na_2SO_4 from Guinama S.L. (Spain). All chemicals were of analytical quality. Deionized and filtered water (Milli-Q Academic®, Millipore, France).

Preparation of the Fe_3O_4 nuclei and the Fe_3O_4/PCL NPs, and GEM loading

Fe_3O_4 nanocores (≈ 10 nm in diameter) were prepared by chemical co-precipitation.[33,34] The Fe_3O_4/PCL particles (of 2:4 Fe_3O_4:PCL weight ratio) were formulated by an interfacial polymer disposition method, generating an adequate size and production performance (PP): ≈ 126 nm and ≈ 91 %, respectively.[14] The NP PP (%) values were calculated by Eq. 1.

$$PP\ (\%) = \frac{\text{amount of NPs obtained (mg)}}{\text{summation of materials used in the preparation of these NPs (mg)}} \times 100$$

(1)

Finally, GEM-loaded particles were obtained by dissolving the chemotherapeutic (up to 1 mM) in 12.5 mL of a 2 % (w/v)

aqueous solution of Kolliphor® P-188 containing the Fe_3O_4 nuclei (0.125 %, w/v), before incorporation of 5 mL of a 1.25 % (w/v) solution of PCL in DCM under mechanical stirring (1200 rpm) (IKA® Eurostar 60 Digital Constant-Speed Mixer, IKA, Germany).[14]

Surface functionalization of the Fe_3O_4/PCL NPs with CS

The Fe_3O_4/PCL nanostructures were surface functionalized with CS by following a coacervation procedure.[28,31,35] The procedure started with the preparation of 25 mL of acetic acid (2 %, v/v) containing CS (0.05, w/v), Fe_3O_4/PCL NPs (0.1 %, w/v), and Kolliphor® P-188 (1 %, w/v). Then, 6.25 mL of a Na_2SO_4 solution (20 %, w/v) were poured under sonication (cycle of 40 %, sonication output of 20 %, and sonication time of 15 min; Branson Sonifier 450, Emerson Electric Co., USA) to obtain the aqueous dispersion of NPs. Finally, the particles were repetitively cleaned by magnetic separation (magnet of 400 mT) until conductivity of the supernatant was ≤10 μS/cm. Formulation of the GEM-loaded (Fe_3O_4/PCL)/CS particles was done by using the GEM-loaded NPs prepared previously (Fig. 1).

CS NPs were also obtained by coacervation, but cleaned by repeated cycles of centrifugation (40 min at 9000 rpm, Centrikon T-124 centrifuge, Kontron, France), until conductivity of the supernatant was ≤10 μS/cm.

Characterization

Determinations of the size (and polydispersity index, PdI) and zeta potential (ζ) of the particles in water (≈ 0.1 %, w/v) were done at 25.0 ± 0.5 °C and by DLS and electrophoresis, respectively (Zetasizer Nano-ZS, Malvern Instruments Ltd., UK).

CS disposition onto the surface of the core/shell NPs was qualitatively characterized by electrophoresis: effect of the ionic strength (fixed with KNO_3 concentrations) on the ζ values of the Fe_3O_4/PCL, CS, and (Fe_3O_4/PCL)/CS NPs particles was investigated at room temperature, being the pH values ≈ 6. Surface functionalization of the core/shell particles with CS was further investigated by FTIR spectrometry (FT/IR-6200 spectrometer, JASCO, USA). Relevant bands of the nanostructure were identified by comparison with published data.[14,31,36,37]

Visualization of the NPs was possible by high resolution transmission electron microscopy (HRTEM), annular bright field scanning transmission electron microscopy (ABF-STEM), and high-angle annular dark field scanning transmission electron microscopy (HAADF-STEM) (Titan G2 60–300 FEI microscope, Thermofisher Scientific Inc., USA). During the electron microscopy characterizations, elemental analysis was accomplished [energy dispersive X-ray (EDX) spectrometer, Bruker Nano GmbH, Germany].

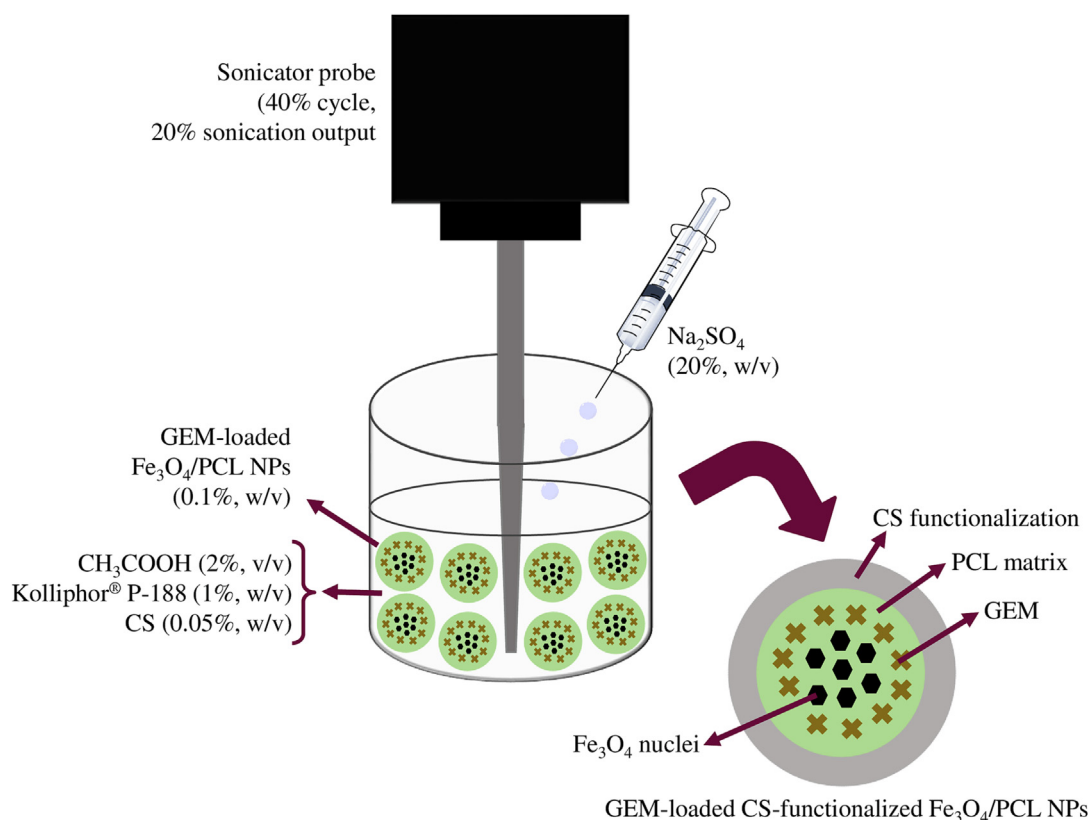Short-term stability of the Fe_3O_4/PCL, and CS-functionalized Fe_3O_4/PCL colloids (1 mg/mL, pH ≈ 6) at 4.0 ± 0.5 °C was

Fig. 1. Preparation of GEM-loaded (Fe_3O_4/PCL)/CS NPs.

tested. Evolution of size, PdI and ζ values of the NPs was measured as a function of time following storage.

Magnetic responsiveness of the $(Fe_3O_4/PCL)/CS$ particles was investigated by determining the hysteresis cycle (Manics DSM-8 vibrating magnetometer, France). Then, the magnetism of the colloid (≈ 0.5 %, w/v) under the influence of a 0.4 T magnet was visualized. These characterizations were done at room temperature.

r_1 and r_2 relaxivities of the $(Fe_3O_4/PCL)/CS$ particles were characterized at a field strength characteristic of clinical systems (≈ 1.5 T), and at 37.0 ± 0.5 °C (Bruker Minispec MQ-60 spectrometer, Bruker BioSpin, Germany).[28] The longitudinal (or spin-lattice) relaxation time (T_1) was determined using the standard inversion-recovery pulse sequence, and the transverse (or spin-spin) relaxation time (T_2) was quantified by standard Carr-Purcell-Meiboom-Gill (CPMG) pulse sequence.

Fe content of the $(Fe_3O_4/PCL)/CS$ NPs was quantified by ICP-HRMS (Element XR High Resolution ICP-MS system, ThermoFisher Scientific Inc., USA).[28]

In vitro cytotoxicity of the (Fe₃O₄/PCL)/CS NPs

The $(Fe_3O_4/PCL)/CS$ particles were tested in HFF-1 human foreskin fibroblasts (American Type Culture Collection, USA). Cell viability was assayed by the MTT proliferation assay. The methodology was previously described.[28,38] Cells in PBS were used as negative controls, while Triton® X-100 (1 %, v/v) was added to the positive controls. Relative cell viability (RCV, %) and the error related to controls were calculated by Eqs. 2 and 3, respectively.

$$RCV\ (\%) = \frac{A_{\text{test}} - A_{\text{positive controls for the NPs}}}{A_{\text{negative controls for the NPs}} - A_{\text{positive controls for the NPs}}} \times 100 \quad (2)$$

$$Error\ (\%) = RCV_{\text{test}} \times \sqrt{\left(\frac{\text{test}}{A_{\text{test}}}\right)^2 + \left(\frac{\text{control}}{A_{\text{control}}}\right)^2} \quad (3)$$

where A is the absorbance, and σ is the standard deviation (SD).

HFF-1 cells were also cultured for cell morphology studies done by confocal microscopy (Operetta® High Content Imaging System, Perkin Elmer, USA).[38] After 24 h of contact with the particles (0.1 to 100 µg/mL of Fe concentration), Triton® X-100 (1 %, v/v) was added to the positive controls. The wells were stained with DAPI (1:3000 dilution) to label cell nuclei, calcein AM (1:1000 dilution) to evaluate cell activity (intracellular esterase activity), and with TO-PRO®-3 iodide (1:1000 dilution) to label dead cells.

Quantification of GEM loading and release

Following a direct method,[39,40] determination of the loading of the chemotherapeutic started with the digestion of 50 mg of GEM-loaded particles (dried at 35 ± 0.5 °C) in 10 mL of DCM under sonication (Bransonic® ultrasonic bath, Branson Ultrasonics Corporation, USA). Then, GEM molecules were extracted by three repeated cycles of contact with 10 mL of water. The resulting 30 mL of aqueous phase containing the extracted drug were centrifuged to separate undissolved compounds (e.g., the Fe_3O_4 nanocores) (45 min at 9000 rpm; Centrifuge 5804, Eppendorf Ibérica S.L.U., Spain). Finally, the supernatant containing GEM was evaluated by ultraviolet (UV) spectrophotometry at 269 nm (Lambda™ 25 UV/Vis spectrophotometer, PerkinElmer Inc., USA). Good linearity was defined at this wavelength between absorbance and drug concentration data ($r = 0.998$), and the method was validated and verified for precision, accuracy, and linearity.

GEM incorporation to the NPs was determined in terms of entrapment efficiency (EE) (%, Eq. 4), and drug loading (DL) (%, Eq. 5).

$$EE\ (\%) = \frac{\text{Entrapped GEM (mg)}}{\text{total GEM used in the experiments (mg)}} \times 100 \quad (4)$$

$$DL\ (\%) = \frac{\text{Entrapped GEM (mg)}}{\text{GEM-loaded NPs (mg)}} \times 100 \quad (5)$$

Drug release from the $(Fe_3O_4/PCL)/CS$ particles with the higher DLs (≈ 10.8 %, Table 1) was characterized by following the dialysis bag method.[14,31] The in vitro drug release medium reproduced the pH of the bloodstream ($C_6H_8O_7$-Na_2HPO_4 buffer, 7.4 ± 0.1), or the acidic environment in the endosomes and lysosomes of tumor cells ($C_6H_8O_7$-NaOH buffer, pH 5.0 ± 0.1).[41] It was kept either at the normal human body-temperature (37.0 ± 0.5 °C), or at the temperature habitually used for a hyperthermia-triggered drug release (45.0 ± 0.5 °C) (also typical of iron oxide-based NPs used in magnetic fluid hyperthermia against cancer).[20] The dialysis bags (cut-off of 2000 Da, Spectrum® Spectra/Por® 6 dialysis membrane tubing, USA) contained 2 mL of GEM-loaded particles (2 mg/mL of antitumor agent). GEM content in the samples was determined by UV spectrophotometric analysis (at 269 nm), and drug release was calculated by using Eq. 6.

$$GEM\ released\ (\%) = \frac{\text{Amount of GEM released (mg)}}{\text{Amount of GEM loaded to the NPs (mg)}} \times 100 \quad (6)$$

MRI experiments

MRI studies were performed in three male SCID mice.[28] Briefly, $(Fe_3O_4/PCL)/CS$ NPs were administered intravenously at a Fe concentration of 5 mg/kg, and followed by MRI using a Bruker BioSpec® 9.4 T animal MRI system (Bruker BioSpin, Germany). The acquisition scheme was as follows: high resolution T_2-weighted images, quantitative T_2 map, intravenous injection of the NPs, dynamic T_2-weighted imaging sequence (one image every 30 s, total acquisition time 35 min), high resolution T_2-weighted images, and quantitative T_2 map. Finally, in vivo distribution was evaluated by quantitative T_2 mapping up to 24 h. Parametric T_2 maps were calculated with scripts written in-house in Interactive Data Language (IDL, Harris Geospatial Solutions, Inc., USA).

A magnetic tumor targeting proof of concept study was done in mice bearing PC3 prostate tumors. Human PC3 cells were

Table 1
Mean diameter (nm), PdI, and ζ data (mV) of the Fe_3O_4/PCL and CS-decorated Fe_3O_4/PCL particles as a function of time (days); and, loading of GEM (EE and DL, %) to the NPs. Experimental values are expressed as means ± SDs ($n = 3$).

Short-term stability assay						
Time (days)	Fe_3O_4/PCL NPs			CS-decorated Fe_3O_4/PCL NPs		
	Size (nm)	PdI	ζ (mV)	Size (nm)	PdI	ζ (mV)
0	126.5 ± 1.8	0.24 ± 0.01	−15.4 ± 4.1	308.1 ± 3.0	0.24 ± 0.02	28.4 ± 0.6
1	149.9 ± 0.7	0.22 ± 0.01	−15.1 ± 0.6	315.8 ± 2.6	0.19 ± 0.01	32.9 ± 0.2
7	455.7 ± 31.4	0.38 ± 0.02	−5.1 ± 1.5	325.2 ± 0.8	0.18 ± 0.01	30.4 ± 1.2
14	828.5 ± 30.1	0.47 ± 0.04	−2.9 ± 1.2	334.5 ± 2.3	0.17 ± 0.01	31.5 ± 0.2
30	Macroaggregates			323.9 ± 6.2	0.17 ± 0.01	32.9 ± 0.5

GEM incorporation to the NPs		
[GEM] (M)	EE (%)	DL (%)
10^{-5}	12.251 ± 1.482	0.016 ± 0.011
5×10^{-5}	29.662 ± 0.953	0.151 ± 0.011
10^{-4}	49.901 ± 0.202	0.972 ± 0.161
5×10^{-4}	65.654 ± 1.154	5.941 ± 1.142
10^{-3}	84.903 ± 0.142	10.843 ± 3.171

brought to $\approx$ 80 to 90 % confluence in DMEM/F-12 (supplemented with 2 mM L-glutamine, 10 % FBS, and 1 % Penicillin/Streptomycin; 37.0 ± 0.5 °C and 5 % CO_2), being then trypsinized, pelleted, and maintained at 4.0 ± 0.5 °C. Three mice were anesthetized with 1 % isoflurane, and 10^6 cells were implanted in both flanks. When tumor volumes reached $\approx$ 500 mm^3, a 1.3 T magnet was placed on the right flank tumor, leaving the other tumor as control, then the (Fe_3O_4/PCL)/CS particles were intravenously injected (Fe concentration: 5 mg/kg), and exposure to the magnet was maintained for 1 h. Magnetic targeting was evaluated by MRI.[42] High resolution T_2-weighted images and quantitative T_2 maps were acquired before and after the exposure to the magnet. Then, to assess tumor perfusion, a commercial contrast agent (Gadovist®) was intravenously injected and followed by T_1 dynamic contrast-enhanced MRI (DCE-MRI).

All the experiments were approved by the local Animal Care Committee and performed in compliance with the EU Directive 2010/63/EU (2010) and the Spanish legislation for the care and use of laboratory animals (R.D. 53/2013).

Ex vivo histology and toxicity determinations

Tissue samples, including heart, lung, spleen, liver, and kidney, were obtained at one day postinjection of the CS-functionalized Fe_3O_4/PCL NPs. In the case of magnetic targeting experiments, tumor samples were obtained at 1 h postinjection. Samples were stained with PB (or H&E) to visualize Fe deposits (or to assess tissue architecture) and analyzed by optical microscopy.[28]

Statistical analysis

All experiments were performed at least in three independent assays. Statistical analyzes were done using the IBM SPSS Statistics software package (version 26.0; IBM Corporation, USA). Experimental data were expressed as mean value ± SD. Student's t-test or two-way analysis of variance helped to compare results considering 95 % confidence interval. Differences were considered statistically significant at $p < 0.05$.

Results

Characterization

A coacervation methodology was developed to functionalize the surface of the Fe_3O_4/PCL NPs with CS. This high-throughput production procedure (PP = 89.3 ± 9.6 %) led reproducibly to (Fe_3O_4/PCL)/CS nanostructures of $\approx$ 308 nm in size and positively charged ($\zeta \approx$ 28 mV in water) (Table 1).

Disposition of the CS shell onto the surface of the Fe_3O_4/PCL NPs was qualitatively evaluated by electrophoresis. At the natural pH value, pH $\approx$ 6, of the aqueous dispersions of CS, Fe_3O_4/PCL, or (core/shell)/shell particles, the ζ values were determined as a function of the ionic strength (fixed with KNO_3) (Fig. 2a). Similarities were clear between the (Fe_3O_4/PCL)/CS NPs and the CS particles and, hence, efficient coverage of the Fe_3O_4/PCL particles by CS can be postulated.

The characteristic bands of the (Fe_3O_4/PCL)/CS NPs were identified in the FTIR spectrum (Fig. 2b): (A) carbonyl group stretching of a carboxylic acid ($\approx$ 1720 cm^{-1}); (B) carbonyl group stretching vibration of an amine group ($\approx$ 1645 cm^{-1}); (C) carbon nitrogen bond stretching in secondary amides ($\approx$ 1530 cm^{-1}); (D) asymmetric methylene group bending vibration ($\approx$ 1450 and $\approx$ 1375 cm^{-1}); (E) oxygen hydrogen bond bending vibration from carboxylic group ($\approx$ 1340 cm^{-1}); (F) carbon oxygen bond stretching absorption from an hydroxyl group (at $\approx$ 1240 cm^{-1}); (G) C—CO—C bond stretching and bending ($\approx$ 1060 cm^{-1}); (H) medium band from alkanes ($\approx$ 960 cm^{-1}); (I) carbon hydrogen bond rocking vibration characteristic of –CH long chains (at $\approx$ 840 cm^{-1}); and, (J) iron oxygen bond vibration from iron oxides ($\approx$ 600 cm^{-1}).
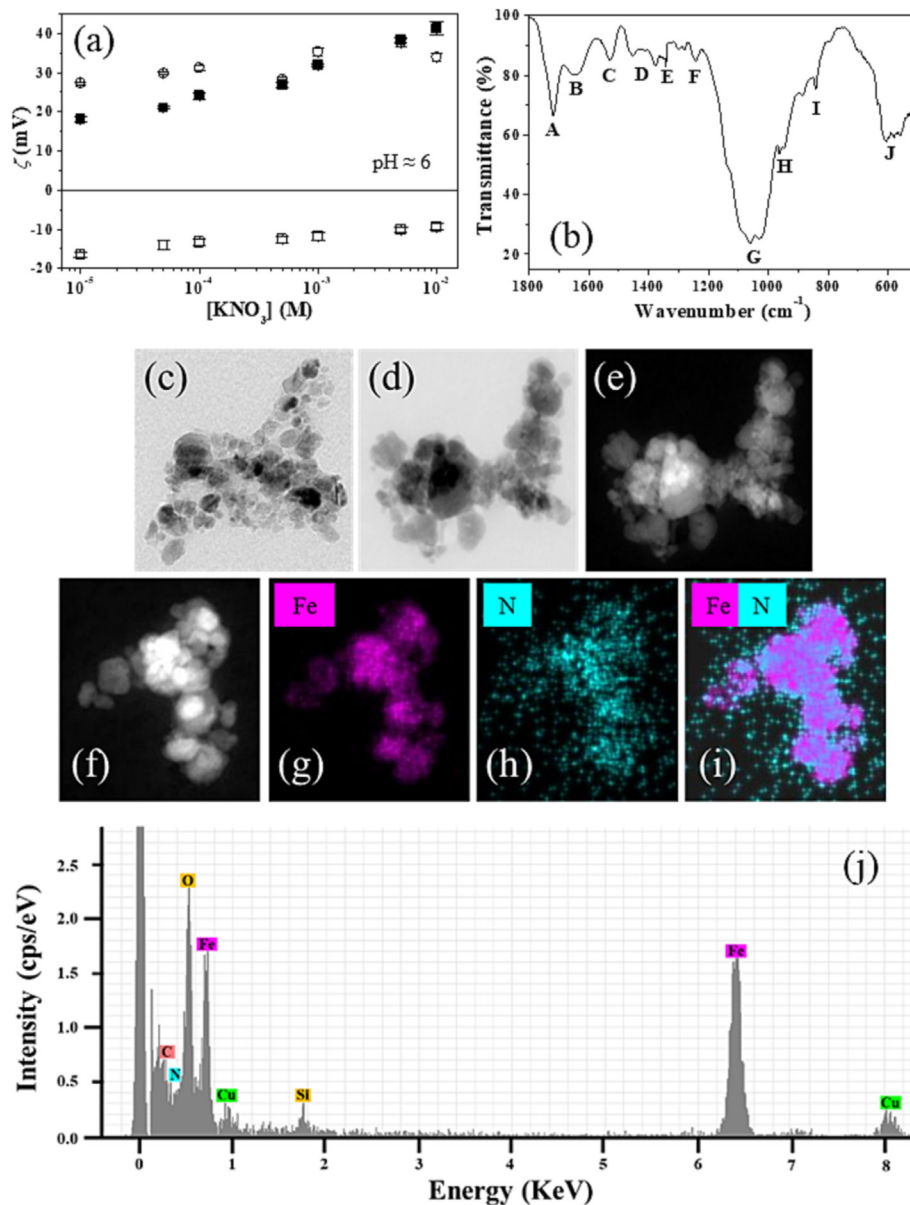
Fig. 2. (*a*) Zeta potential (ζ, mV) of the CS (○), Fe$_3$O$_4$/PCL (□), and (Fe$_3$O$_4$/PCL)/CS (■) particles as a function of KNO$_3$ concentration. (*b*) FTIR spectra of the (Fe$_3$O$_4$/PCL)/CS NPs. (*c*) HRTEM, (*d*) ABF-STEM, and (*e* and *f*) HAADF-STEM images of the (Fe$_3$O$_4$/PCL)/CS NPs; EDX mapping analysis of Fe (*g*), N (*h*), and overlapped Fe and N (*i*) elements of the sample in *f*; and, (*j*) EDX spectra of these particles.

Complete and homogeneous inclusion of the Fe$_3$O$_4$ particles into the PCL nanomatrix surface functionalized by CS was observed by HRTEM, ABF-STEM and HAADF-STEM imaging (Fig. 2c, d, e and f), and by EDX Fe and N element mappings (Fig. 2g, h, and i). Homogeneous distribution of CS onto the Fe$_3$O$_4$/PCL particles was also clear in the Figs. EDX spectra made clear the presence of the C, N, Fe, and O elements for the nanostructure (Fig. 2j). N and Fe came from the CS shell and Fe$_3$O$_4$ nuclei, respectively.

Results from the short-term stability test are detailed in Table 1. Tendency to aggregation is clear for the Fe$_3$O$_4$/PCL NPs, while no relevant changes were observed for the (Fe$_3$O$_4$/PCL)/CS particles.

Hysteresis cycle of the (Fe$_3$O$_4$/PCL)/CS particles is plotted in Fig. 3a. Saturation magnetization and initial susceptibility of the particles were 11.34 ± 0.81 Am^2/kg and $(0.156 \pm 0.026) \times 10^{-3}$ m^3/kg, respectively. The adequate magnetic responsiveness was confirmed qualitatively (Fig. 3b): complete attraction of the particles to a permanent magnet of 0.4 T took place in 2 min.

The possible application of the (Fe$_3$O$_4$/PCL)/CS NPs as T_2 contrast agents in MRI was first demonstrated *in vitro* (Fig. 3c). Their r_1 and r_2 relaxivities were 0.3 and 70.6 mM^{-1} × s^{-1}, respectively. The r_2/r_1 ratio was ≈ 235.

In vitro cytotoxicity

Evaluation of the cytotoxicity of the (core/shell)/shell particles in the HFF-1 line was based on the characterization of the mitochondrial activity, the existence of necrotic or early
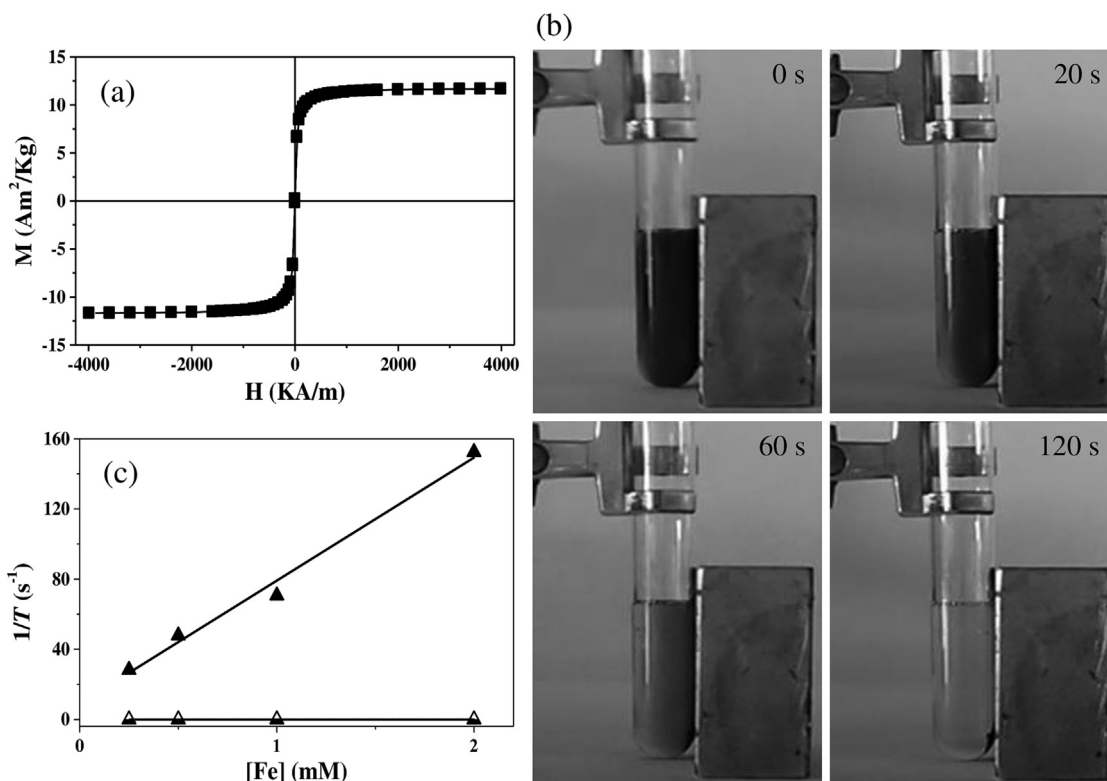
Fig. 3. (*a*) Hysteresis cycle of the (Fe$_3$O$_4$/PCL)/CS particles; (*b*) an aqueous dispersion of these NPs under the influence of a magnet placed close to the right lateral of the vial; and, (*c*) longitudinal (Δ, $1/T_1$, s^{-1}) and transverse ($\blacktriangle$, $1/T_2$, s^{-1}) relaxation rates as a function of Fe concentration in these particles.

apoptotic cells, the intracellular esterase activity, and the cell morphology (Fig. 4). Increasing concentrations of NPs (0.1 to 100 µg/mL of Fe) generated almost null toxicity to the fibroblasts. The CS-functionalized particles did not affect the mitochondrial activity (Fig. 4a, $p < 0.05$), total number of HFF-1 cells (Fig. 4b), percentage of dead cells (Fig. 4c), and calcein activity values (Fig. 4d). However, the total number of HFF-1 cells (Fig. 4b) was only significantly altered at the highest NP concentration ($p < 0.05$). In line with these results, and at the highest concentration of NPs (100 µg/mL of Fe), negligible changes in cell morphology were observed (Fig. 4g).

GEM loading and release properties

The EE (%) and DL (%) of GEM to the (core/shell)/shell NPs was comparable to that of Fe$_3$O$_4$/PCL particles,[14] despite the functionalization of the particle surface by CS (Table 1). Size and surface electrical charge of the NPs were not modified after GEM incorporation: 312.3 ± 3.6 nm and ≈ 30.1 ± 1.9 mV, respectively.

Drug release experiments were first devoted to the definition of the pH-responsive GEM release capabilities of the (Fe$_3$O$_4$/PCL)/CS particles at the normal body temperature (Fig. 5). A biphasic drug release profile took place at the pH 7.4 of bloodstream for the (Fe$_3$O$_4$/PCL)/CS NPs (Fig. 5). The chemotherapeutic was released rapidly during a first burst phase (≈ 28 % in 3 h), while a second slow phase involved the diffusion of the main GEM portion through the polymeric matrices (≈ 72 % in 189 h). On the contrary, GEM release was considerably aug-

mented at the characteristic acidic pH of endosomes and lysosomes of tumor cells, ending after only 48 h. Hence, the pH-responsive GEM release behavior of the (core/shell)/shell nanostructure is apparent in the Figure: ≈ 4-fold faster release at pH 5.0 compared to physiological pH ($p < 0.05$).

Finally, the heat-responsive GEM release capabilities of the NPs were also investigated at pH 7.4, and at pH 5 (Fig. 5). At the magnetic hyperthermia conditions fixed to activate drug release (45.0 ± 0.5 °C),[26,31] GEM release was finished in 8 h at pH 7.4, and in 6 h at pH 5. The heat-responsive drug release behavior of the particles is clear in Fig. 5: ≈ 24-fold and ≈ 31-fold faster release at 45 °C compared to normal body temperature at pH 7.4 and at pH 5, respectively ($p < 0.05$).

In vivo MRI and biodistribution

Upon intravenous injection in SCID mice, short-term pharmacokinetics of the (Fe$_3$O$_4$/PCL)/CS particles was characterized by dynamic MRI (Fig. 6). Rapid liver uptake of the NPs occurred, given the fast relative enhancement increase of ≈ 40 % within ≈ 5 min (Fig. 6a). Lower particle uptakes (increase of ≈ 20 %) were observed for the spleen (Fig. 6b) and kidneys (Fig. 6c). Then, the values of relative enhancement remained steady throughout the experiment (Fig. 6a, b, and c).

Biodistribution of the CS-functionalized Fe$_3$O$_4$/PCL particles was also analyzed qualitatively by T_2-weighted MR images (Fig. 6d, e, and f), and quantitatively by T_2-mapping (Fig. 6g). Clear hypo-intensity areas at 1 and 24 h postinjection were observed in liver, kidneys, and spleen images (Fig. 6d, e, and f).
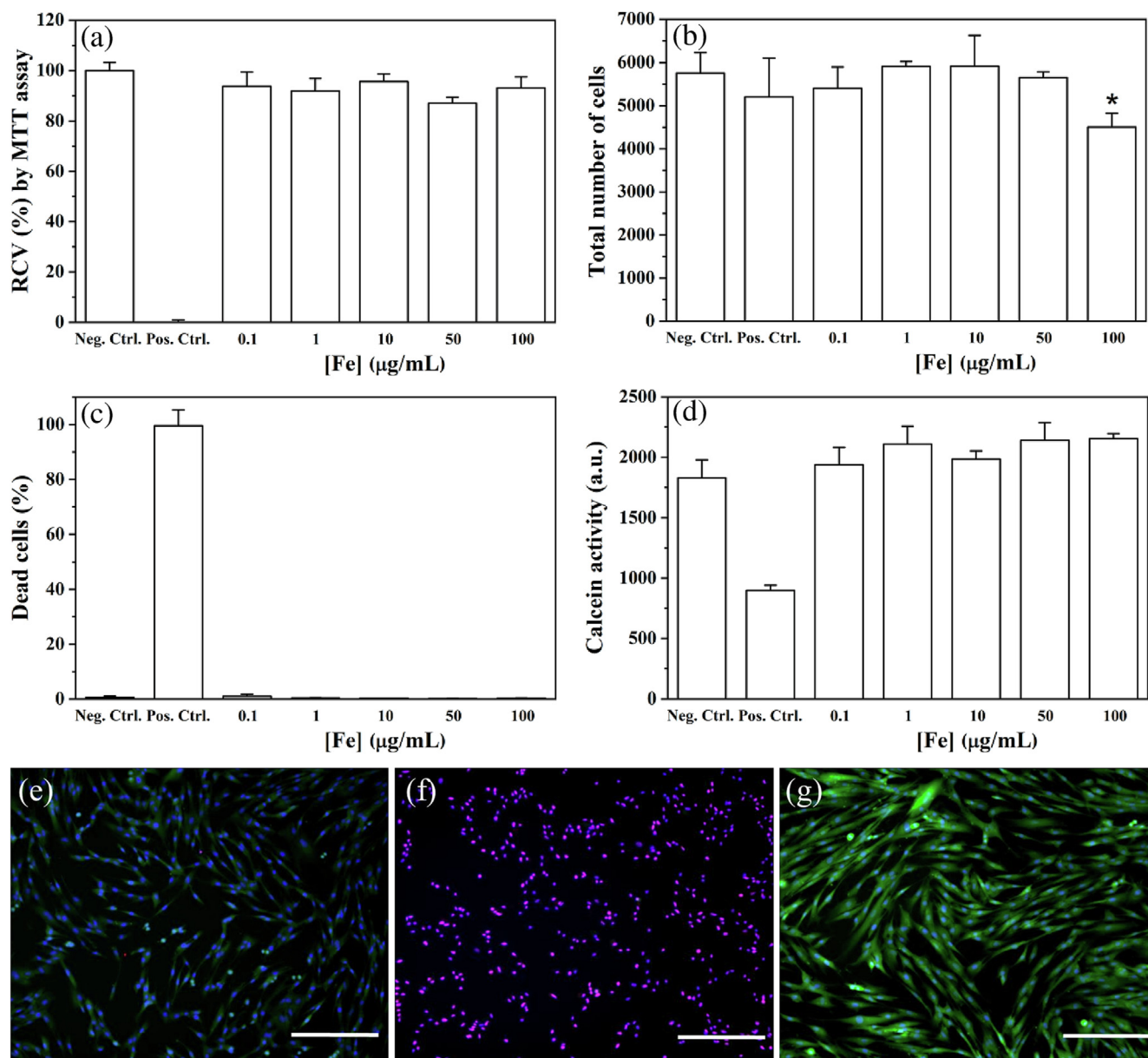
Fig. 4. (*a*) Relative cell viability (RCV, %) by MTT assay, (*b*) total number of cells, (*c*) dead cells (%), and (*d*) calcein activity (arbitrary units, a. u.) of HFF-1 fibroblasts, after contact with increasing concentrations of (Fe$_3$O$_4$/PCL)/CS particles. Representative confocal microscopy images of HFF-1 fibroblasts: negative controls (Neg. Ctrl., *e*), positive controls (Pos. Ctrl., *f*), and cells exposed to the NPs (*g*, 100 μg/mL of Fe). DAPI (blue), TO-PRO®-3 iodide (red) and calcein AM (green) are merged in these images. Bar lengths: 100 μm. The statistical test was significant for data with * ($p < 0.05$).

However, quantitative T_2-mapping revealed that only liver and kidneys exhibited statistically significant increases in R_2 ($1/T_2$, $p < 0.05$), with $\Delta R_2 \approx 3.9$ and ≈ 8.0 s^{-1} at 1 h postinjection, and ≈ 8.9 and ≈ 15.7 s^{-1} at 24 h postinjection, respectively. No significant T_2 changes were observed at any time in the muscle.

Magnetic tumor targeting

Fig. 7a illustrates how the external magnetic field was placed exclusively on the right flank tumor of PC3 prostate tumor-bearing mice. This experimental design, with two tumors per animal, allowed to compare passive *vs.* active tumor targeting in the same mouse (external magnetic field-induced selective *in vivo* distribution of the CS-functionalized NPs at 1 h post-administration). Notable darkening, or decrease in T_2 signal, was detected only at the areas of the tumor close to the 1.3 T permanent magnet, while almost null darkening characterized the rest of the tumor mass (and control tumor) (Fig. 7b). Parametric T_2 maps before and after the administration of the NPs revealed a statistically significant increase in R_2 or $1/T_2$ ($\Delta T_2 \approx 1.5$ s^{-1}) in the tumor periphery compared to other areas (and control tumor) (Fig. 7c).
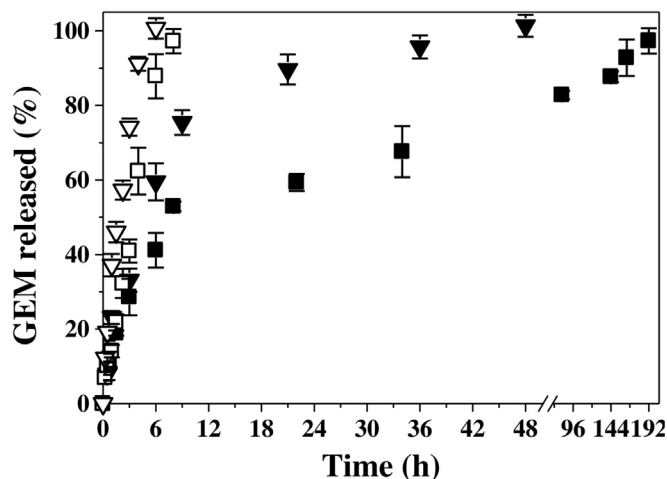
Fig. 5. Release of GEM (%) from the (Fe$_3$O$_4$/PCL)/CS NPs as a function of the incubation time (h) at pH 7.4 ± 0.1 and 37.0 ± 0.5 °C (■), pH 5.0 ± 0.1 and 37.0 ± 0.5 °C (▼), pH 7.4 ± 0.1 and 45.0 ± 0.5 °C (□), and pH 5.0 ± 0.1 and 45.0 ± 0.5 °C (∇).

The (Fe$_3$O$_4$/PCL)/CS particles were detectable by PB staining only a few hundred microns deep from where the magnet was placed (Fig. 7d). On the contrary, no Fe deposits were visualized at the control tumor mass (Fig. 7e).

Finally, the tumor vascular permeability was assessed by T_1 DCE-MRI, after the intravenous injection of Gadovist® (Fig. 7f). Similar behavior was observed in both tumors, either considering the whole tumor (Fig. 7g) or the tumor periphery (Fig. 7h).

Ex vivo histology evaluation of iron deposits, and toxicity assessment

Fig. 8a collects PB staining pictures of liver, kidney and lung tissue samples of a SCID mouse at 24 h post-administration of the (core/shell)/shell particles. In agreement with findings described in the *In vivo* MRI and biodistribution section, Fe deposits were observed in liver (principally in Kupffer cells) and kidneys, while null accumulation was detected in lungs.
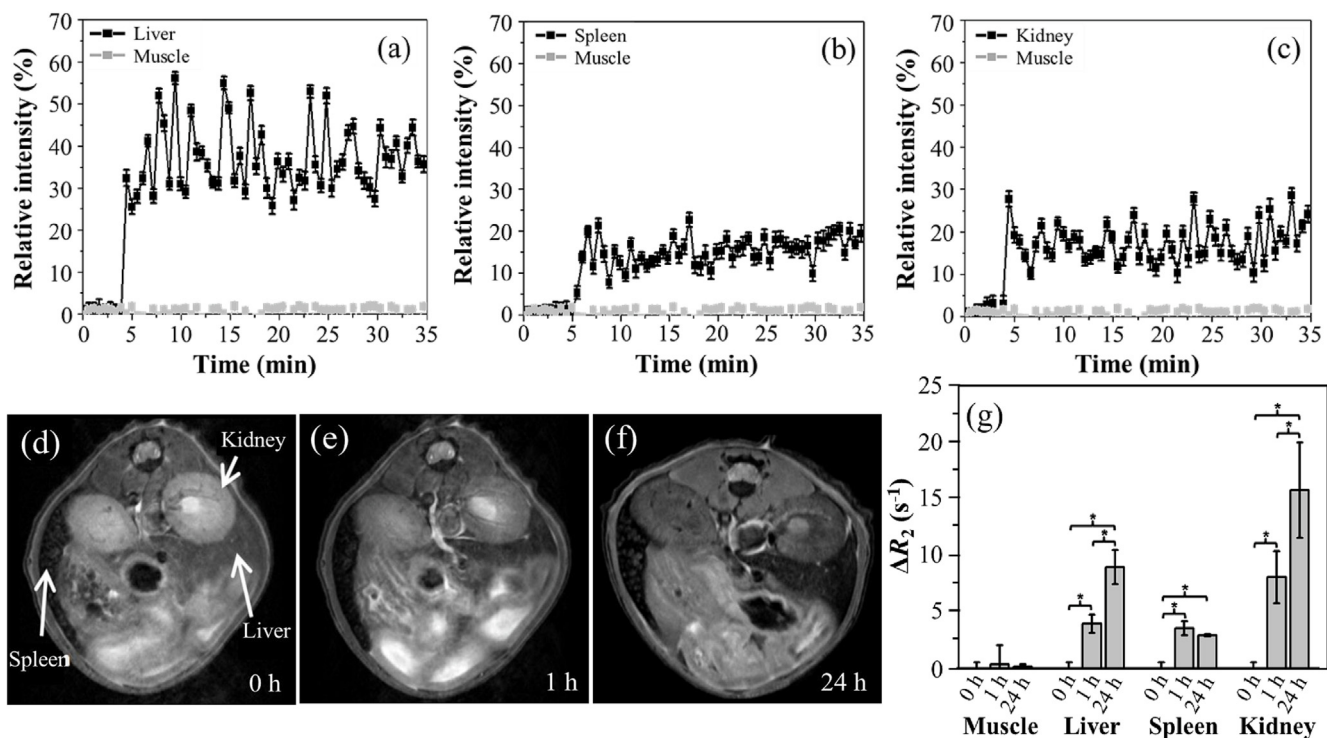
Fig. 6. *In vivo* time courses of the (Fe$_3$O$_4$/PCL)/CS particles: (*a*) liver; (*b*) spleen; and, (*c*) kidney. Representative T_2-weighted MR images of kidney, spleen, and liver after NP injection at: (*d*) 0, (*e*) 1, and (*f*) 24 h. (*g*) ΔR_2 (s^{-1}) as a function of time (h) of muscle, liver, spleen and kidney after NP injection. The statistical test was significant for data with * ($p < 0.05$).
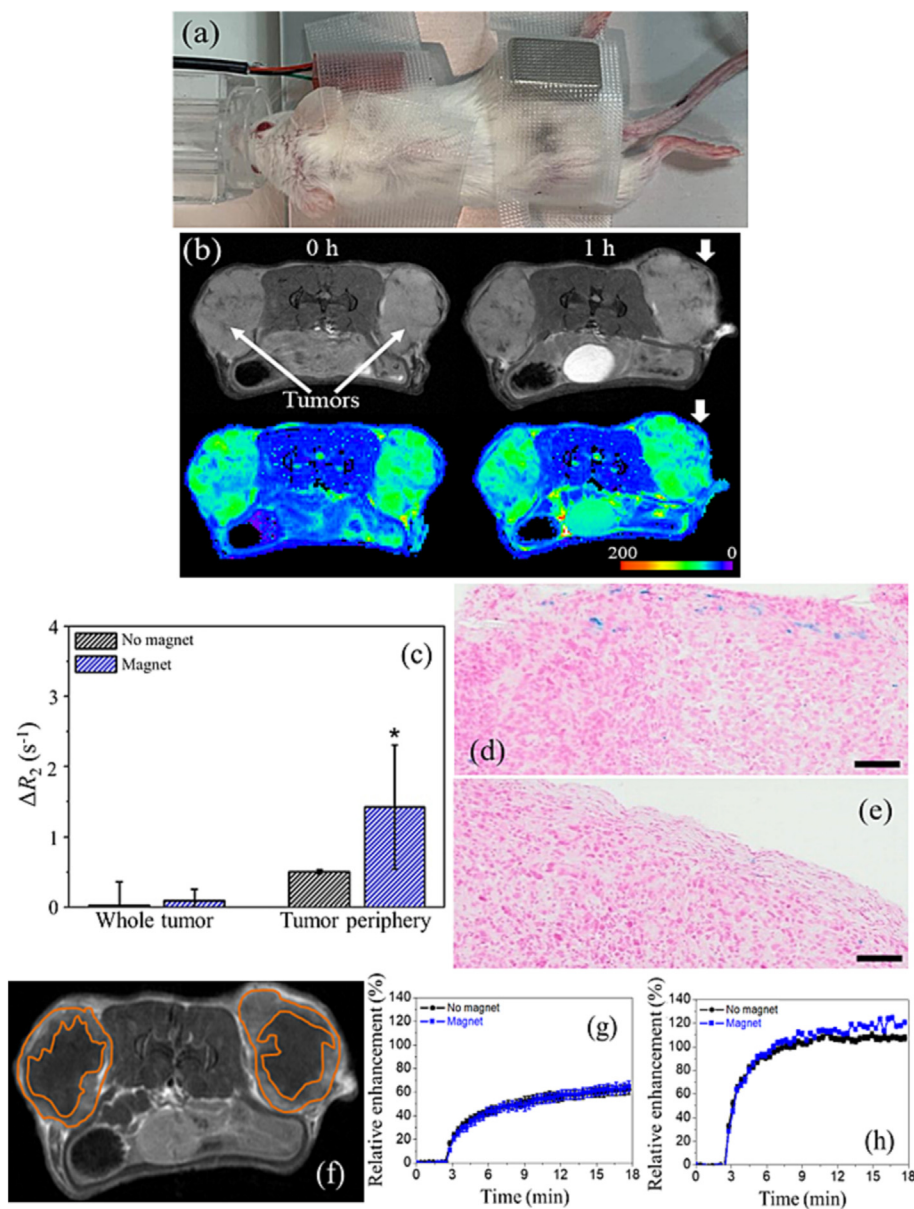
Fig. 7. (*a*) Magnetic tumor targeting proof of concept experiment. (*b*) Representative T_2-weighted MR images (top) and parametric T_2 maps (bottom) at 0 and 1 h after NP injection. Thick arrows indicate main zones of magnetically-guided accumulation of the NPs (tumor periphery). (*c*) ΔR_2 (s^{-1}) at the whole tumor or tumor periphery at 1 h post-intravenous administration of the NPs, calculated from the quantitative T_2 map analysis. Differences were considered statistically significant at $p < 0.01$ (*), compared to 0 h. PB staining of histological sections of the tumors, 1 h after NP administration, and with (*d*) and without (*e*) magnetic targeting. Bar lengths: 100 μm. Representative T_1-weighted MR image (*f*), and short-term MRI characterization of the distribution of Gadovist® in the whole tumor (*g*) and tumor periphery (*h*), drawn with orange lines, after its intravenous administration. Blue lines in *g* and *h* refer exclusively to the tumors where the NPs were targeted magnetically before. Differences in the values (%) could be attributed to minor vascularization differences in the area selected manually, that could contain a necrotic zone where Gadovist® may show a slower enhancement curve.

To continue with the characterization of the toxicity of the $(Fe_3O_4/PCL)/CS$ NPs, H&E staining optical microscopy images were taken of liver, kidney, spleen, lung and heart tissue samples at 24 h post-intravenous administration (Fig. 8b). Swelling with cytoplasmic vacuolation, a frequent sign of mild acute and subacute liver injury, was not detected in liver sections. Normal kidney sections were observed with normal tubular brush-borders and intact glomerulus and surrounding Bowman's capsule. In accordance with these findings, no toxicity was observed in spleen, lungs, and heart.

Finally, tumor sections were stained with H&E to define the internal architecture of the malignant tissue (Fig. 8c). Neither the NPs nor the external magnet induced a change on the tissue architecture.

Discussion

Engineering of antitumor theranostics is habitually associated to complex synthesis routes involving low production performances. In this work, it is detailed a reproducible, easy and efficient procedure to
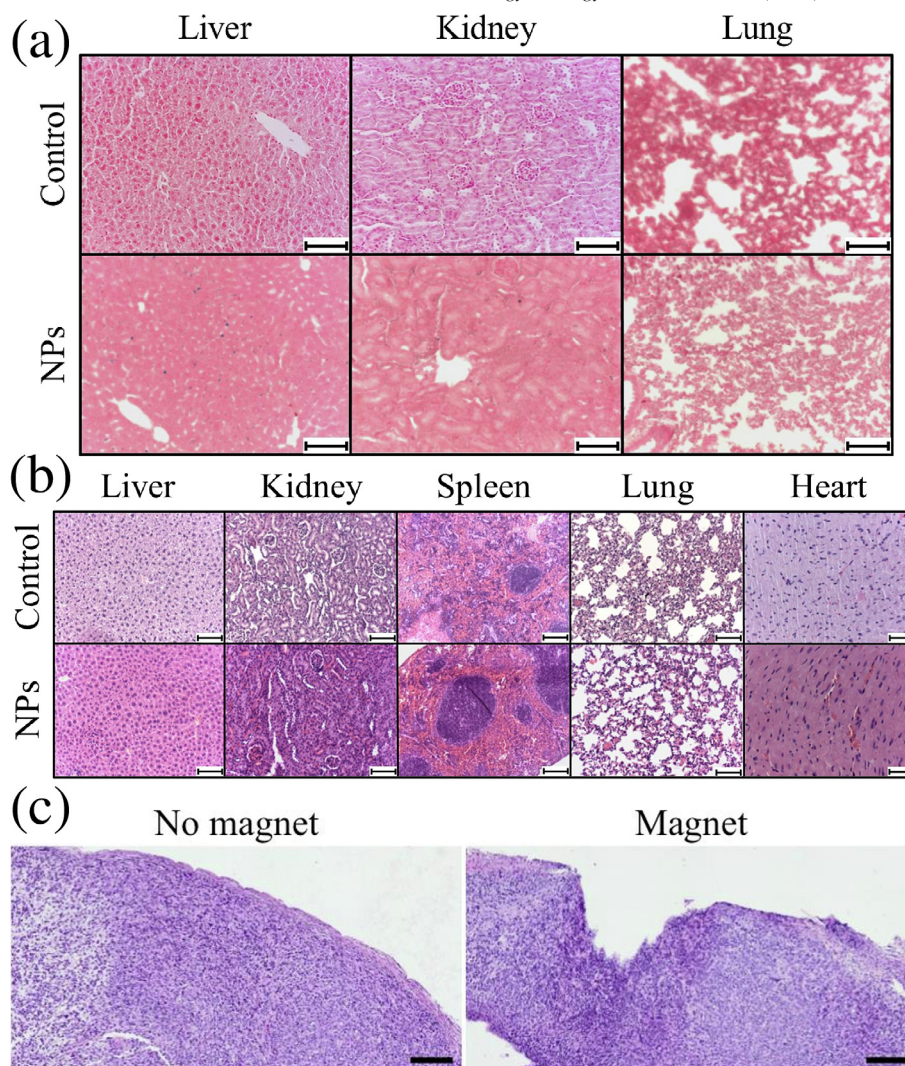
Fig. 8. (a) PB and (b) H&E stainings of representative histological sections of controls, and liver, kidney, spleen, lung and heart at 24 h post-intravenous administration of the (Fe$_3$O$_4$/PCL)/CS NPs. Bar lengths: 100 μm. (c) H&E stainings of histological sections of the tumors, 1 h after NP postinjection, and without and with magnetic targeting. Bar lengths: 200 μm.

formulate positively charged CS-functionalized Fe$_3$O$_4$/PCL NPs. That (core/shell)/shell nanoconformation was defined by electrophoretic, Fourier transform infrared, electron microscopy, and EDX analysis. Size ($\approx$ 308 nm) and surface electrical charge ($\zeta \approx$ 28 mV) have been described to retard opsonization and to prevent fast clearance of nanomedicines from blood by the mononuclear phagocyte system (MPS).[20,43] As a consequence, these (core/shell)/shell NPs could reach the malignant cells by entering through the pores at the leaky tumor vessels (from 100 nm to 2 μm in size).[44] In addition, the positive surface electrical charge, generated by the amino groups in the CS structure,[31] is expected to favor the internalization of these NPs by negatively charged tumor cells.[29]

The electrokinetic characterization could be used also to hypothesize the mechanism of functionalization of the PCL surface in the core/shell particles by CS: attractive interactions between these negatively and positively charged polymers.

Results from a short-term stability study highlighted the need for the CS surface functionalization to prevent NP aggregation. In fact, tendency to aggregation was clear for the Fe$_3$O$_4$/PCL particles, probably the consequence of an inefficient electrostatic repulsion between particles displaying relatively low ζ values.[20] On the contrary, CS functionalization on these core/shell particles was stable during storage, and provided stability to the resulting colloid: no relevant change in size and surface electrical charge was detected during the study. The greater surface electrical charge and hydrophilic character of the CS-functionalized particles may determine relevant electrostatic repulsions between particles and, thus, colloidal stability.[20,27,28]

In vitro experiments demonstrated that the (Fe$_3$O$_4$/PCL)/CS particles may display appropriate superparamagnetic behavior and good properties as T_2 contrast agents in MRI. Firstly, given that the hysteresis behavior was not present in the hysteresis cycle, the NPs could not have remnant magnetization, and thus they are expected to display a superparamagnetic character.[20,45] Secondly, r_1 and r_2 relaxivities were similar to analogous T_2 nanostructures,[20,28] and contrast agents, *e.g.*, Ferumoxytol.[46] The r_2/r_1 ratio ($\approx$ 235) further suggested the potential use of the CS-functionalized NPs as T_2 contrast agents.[47]

In vitro and *ex vivo* toxicity tests suggested the safety for the biomedical use of the nanostructure. For example, evaluation of the cytotoxicity of the particles in the HFF-1 line reported RCV (%) values always higher than 80 %, relative to negative controls. These results demonstrate that the $(Fe_3O_4/PCL)/CS$ NPs themselves are non-toxic, according to ISO-10993-5.[48] In addition, tumor sections stained with H&E exhibited high cellularity and dense cell packing, characteristics in agreement with previously reported PC3 tissular conformations.[49]

One of the main limitations to successful GEM-based chemotherapy is the rapid elimination of this antitumor agent, being thus the plasma half-life $\approx$ 5 to 20 min.[50] The formulation of GEM-loaded nanocarriers, including PCL-based NPs, has been described to improve *in vitro* and *in vivo* the efficacy and safety of this chemotherapeutic, by controlling drug release and focusing their distribution specifically inside malignant cells.[51] Therefore, formulation conditions were carefully defined to assure an adequate mechanical trapping of this drug within the PCL matrix, as previously described.[14] The biphasic drug release profile from the $(Fe_3O_4/PCL)/CS$ occurring at the pH 7.4 of bloodstream is characteristic of PCL,[14,52] CS,[32,53] and CS-PCL matrices.[54] More interestingly, incorporation of GEM to the NPs gained benefits from a dual pH- and heat-responsive release behavior. Both, the PCL matrix in which the drug was embedded, and the CS surface coating onto the core/shell nanostructure, have been described to be pH-responsive materials.[14,23,32] In addition, the PCL matrix, in which the GEM molecules were embedded, has been described to be a temperature-sensitive polymer.[24,25] Thus, GEM release was significantly accelerated at the magnetic hyperthermia conditions fixed to activate drug release (45.0 ± 0.5 °C).[26,31]

Considering the properties represented in the Figs. 3 and 5, it could be postulated that the $(Fe_3O_4/PCL)/CS$ NPs are magnetic-, pH- and heat (hyperthermia)-responsive nanostructures that may optimize the concentration of GEM into the tumor cells.[20,55]

Thanks to the good characteristics of the $(Fe_3O_4/PCL)/CS$ particles as T_2 contrast agents, analysis of the *in vivo* distribution of the NPs was possible by MRI, comparing passive *vs.* active (magnetic) tumor targeting. It was defined an inefficient passive targeting of the particles, while NP delivery to the tumor site was improved when applying an external magnetic field. The results emphasize the limitations of the enhanced permeability and retention effect, being they associated to the dependency of the effect on the tumor type and location. In the absence of a magnetic field to control biodistribution, rapid liver uptake of the NPs occurred while part of them was also retained in kidneys, given their size.[56] Taken together, these results suggest that the $(Fe_3O_4/PCL)/CS$ particles are rapidly recognized by the MPS and removed from the bloodstream by Kupffer cells and, to a less extent, by splenic macrophages.

Regarding the magnetic tumor targeting experiment, findings indicate that a magnetically guided accumulation of the $(Fe_3O_4/PCL)/CS$ particles occurred at the tumor surface. Parametric T_2 maps before and after the administration of the NPs supported this hypothesis. PB staining confirmed also that NP accumulation was not a consequence of passive targeting, since it only took place clearly in the tumor under the influence of the magnetic field. Hence, differences in NP accumulation could be attributed to the effect of the external magnet, and not to variances in vascular permeability. The results are in agreement with a previous magnetic tumor targeting study,[57] while highlighting the priorly reported limitations of the enhanced permeability and retention effect (associated to the dependency of the effect on the tumor type and location).[58,59] These findings were in accordance with: *i*) the poor tumor vascular permeability to the (core/shell)/shell particles verified by T_1 DCE-MRI using Gadovist® and H&E stained tumor sections; and, *ii*) the *in vivo* distribution of similar NPs (surface functionalized with chitosan and $\approx$ 300 nm in size).[60] Thus, magnetic targeting may enhance the accumulation of NPs even in tumors where negligible passive targeting is expected.

Finally, it could be postulated that these (core/shell)/shell particles may constitute a potential theranostic nanotool (biomedical imaging & chemotherapy) against solid tumors. Additional *in vitro*, *ex vivo* and *in vivo* experiments are needed to provide conclusive evidence of the biocompatibility, safety, and therapeutic possibilities of such promising multi-stimuli-responsive nanostructure.

Funding

CRediT authorship contribution statement

Gracia García-García: Methodology, Investigation, Formal analysis, Writing – original draft. **Carlos Caro:** Methodology, Investigation, Formal analysis, Writing – original draft. **Fátima Fernández-Álvarez:** Investigation, Formal analysis. **María Luisa García-Martín:** Conceptualization, Methodology, Formal analysis, Resources, Writing – review & editing. **José L. Arias:** Conceptualization, Methodology, Formal analysis, Resources, Writing – original draft, Writing – review & editing, Supervision.

Declaration of competing interest

The authors declare no competing interests.

Acknowledgements

References

1. Beutel AK, Halbrook CJ. Barriers and opportunities for gemcitabine in pancreatic cancer therapy. *Am J Physiol Cell Physiol* 2023;**324**: C540-52, https://doi.org/10.1152/ajpcell.00331.2022.

2. Zhu L, Chen R, Yang Q, Liu H, Zheng Q, Li L. Modelling an evaluation of the efficacy and safety of gemcitabine combined with platinum in the treatment of non-small cell lung cancer. *J Clin Pharm Ther* 2022;**47**: 986-94, https://doi.org/10.1111/jcpt.13632.

3. Hertel LW, Boder GB, Kroin JS, Rinzel SM, Poore GA, Todd GC, et al. Evaluation of the antitumor activity of gemcitabine (2′,2′-difluoro-2′-deoxycytidine). *Cancer Res* 1990;**50**:4417-22.

4. Sehouli J. Review of gemcitabine-based combinations for platinum-resistant ovarian cancer. *Int J Gynecol Cancer* 2005;**15**(suppl 1):23-30, https://doi.org/10.1111/j.1525-1438.2005.15353.x.

5. Kawada T, Yanagisawa T, Araki M, Pradere B, Shariat SF. Sequential intravesical gemcitabine and docetaxel therapy in patients with nonmuscle invasive bladder cancer: a systematic review and meta-analysis. *Curr Opin Urol* 2023;**33**:211-8, https://doi.org/10.1097/MOU.0000000000001065.

6. Dubey RD, Saneja A, Gupta PK, Gupta PN. Recent advances in drug delivery strategies for improved therapeutic efficacy of gemcitabine. *Eur J Pharm Sci* 2016;**93**:147-62, https://doi.org/10.1016/j.ejps.2016.08.021.

7. Dessale M, Mengistu G, Mengist HM. Nanotechnology: a promising approach for cancer diagnosis, therapeutics and theragnosis. *Int J Nanomed* 2022;**17**:3735-49, https://doi.org/10.2147/IJN.S378074.

8. Jin KT, Yao JY, Ying XJ, Lin Y, Chen YF. Nanomedicine and early cancer diagnosis: molecular imaging using fluorescence nanoparticles. *Curr Top Med Chem* 2020;**20**:2737-61, https://doi.org/10.2174/1568026620666200922112640.

9. Rawal S, Patel MM. Threatening cancer with nanoparticle aided combination oncotherapy. *J Control Release* 2019;**301**:76-109, https://doi.org/10.1016/j.jconrel.2019.03.015.

10. Xin Y, Huang M, Guo WW, Huang Q, Zhang LZ, Jiang G. Nano-based delivery of RNAi in cancer therapy. *Mol Cancer* 2017;**16**:134, https://doi.org/10.1186/s12943-017-0683-y.

11. Zhen X, Cheng P, Pu K. Recent advances in cell membrane-camouflaged nanoparticles for cancer phototherapy. *Small* 2019;**15**e1804105, https://doi.org/10.1002/smll.201804105.

12. Kang JK, Kim JC, Shin Y, Han SM, Won WR, Her J, et al. Principles and applications of nanomaterial-based hyperthermia in cancer therapy. *Arch Pharm Res* 2020;**43**:46-57, https://doi.org/10.1007/s12272-020-01206-5.

13. Chan L, Huang Y, Chen T. Cancer-targeted tri-block copolymer nanoparticles as payloads of metal complexes to achieve enhanced cancer theranosis. *J Mater Chem B* 2016;**4**:4517-25, https://doi.org/10.1039/c6tb00514d.

14. García-García G, Fernández-Álvarez F, Cabeza L, Delgado ÁV, Melguizo C, Prados JC, et al. Gemcitabine-loaded magnetically responsive poly(ε-caprolactone) nanoparticles against breast cancer. *Polymers (Basel)* 2020;**12**:2790, https://doi.org/10.3390/polym12122790.

15. Muñoz de Escalona M, Sáez-Fernández E, Prados JC, Melguizo C, Arias JL. Magnetic solid lipid nanoparticles in hyperthermia against colon cancer. *Int J Pharm* 2016;**504**:11-9, https://doi.org/10.1016/j.ijpharm.2016.03.005.

16. Shi J, Kantoff PW, Wooster R, Farokhzad OC. Cancer nanomedicine: progress, challenges and opportunities. *Nat Rev Cancer* 2017;**17**:20-37, https://doi.org/10.1038/nrc.2016.108.

17. Etemadi H, Buchanan JK, Kandile NG, Plieger PG. Iron oxide nanoparticles: physicochemical characteristics and historical developments to commercialization for potential technological applications. *ACS Biomater Sci Eng* 2021;**7**:5432-50, https://doi.org/10.1021/acsbiomaterials.1c00938.

18. Pérez-Artacho B, Gallardo V, Ruiz MA, Arias JL. Maghemite/poly(D,L-lactide-co-glycolyde) composite nanoplatform for therapeutic applications. *J Nanopart Res* 2012;**14**:768, https://doi.org/10.1007/s11051-012-0768-x.

19. Arias JL, Reddy LH, Couvreur P. Fe₃O₄/chitosan nanocomposite for magnetic drug targeting to cancer. *J Mater Chem* 2012;**22**:7622-32, https://doi.org/10.1039/C2JM15339D.

20. Reddy LH, Arias JL, Nicolas J, Couvreur P. Magnetic nanoparticles: design and characterization, toxicity and biocompatibility, pharmaceutical and biomedical applications. *Chem Rev* 2012;**112**:5818-78, https://doi.org/10.1021/cr300068p.

21. Kim D, Shin K, Kwon SG, Hyeon T. Synthesis and biomedical applications of multifunctional nanoparticles. *Adv Mater* 2018;**30**e1802309, https://doi.org/10.1002/adma.201802309.

22. Nottelet B, Darcos V, Coudane J. Aliphatic polyesters for medical imaging and theranostic applications. *Eur J Pharm Biopharm* 2015;**97**: 350-70, https://doi.org/10.1016/j.ejpb.2015.06.023.

23. Deirram N, Zhang C, Kermaniyan SS, Johnston APR, Such GK. pH-responsive polymer nanoparticles for drug delivery. *Macromol Rapid Commun* 2019;**40**e1800917, https://doi.org/10.1002/marc.201800917.

24. Wang W, Deng L, Liu S, Li X, Zhao X, Hu R, et al. Adjustable degradation and drug release of a thermosensitive hydrogel based on a pendant cyclic ether modified poly(ε-caprolactone) and poly(ethylene glycol)co-polymer. *Acta Biomater* 2012;**8**:3963-73, https://doi.org/10.1016/j.actbio.2012.07.021.

25. Bartnikowski M, Dargaville TR, Ivanovski S, Hutmacher DW. Degradation mechanisms of polycaprolactone in the context of chemistry, geometry and environment. *Prog Polym Sci* 2019;**96**:1-20, https://doi.org/10.1016/j.progpolymsci.2019.05.004.

26. Kiamohammadi L, Asadi L, Shirvalilou S, Khoei S, Khoee S, Soleymani M, et al. Physical and biological properties of 5-fluorouracil polymer-coated magnetite nanographene oxide as a new thermosensitizer for alternative magnetic hyperthermia and a magnetic resonance imaging contrast agent: in vitro and in vivo study. *ACS Omega* 2021;**6**: 20192-204, https://doi.org/10.1021/acsomega.1c01763.

27. Voon SH, Tiew SX, Kue CS, Lee HB, Kiew LV, Misran M, et al. Chitosan-coated poly(lactic-co-glycolic acid)-diiodinated boron-dipyrromethene nanoparticles improve tumor selectivity and stealth properties in photodynamic cancer therapy. *J Biomed Nanotechnol* 2016;**12**: 1431-52, https://doi.org/10.1166/jbn.2016.2263.

28. Fernández-Álvarez F, Caro C, García-García G, García-Martín ML, Arias JL. Engineering of stealth (maghemite/PLGA)/chitosan (core/shell)/shell nanocomposites with potential applications for combined MRI and hyperthermia against cancer. *J Mater Chem B* 2021;**9**:4963-80, https://doi.org/10.1039/d1tb00354b.

29. Seidi F, Jenjob R, Phakkeeree T, Crespy D. Saccharides, oligosaccharides, and polysaccharides nanoparticles for biomedical applications. *J Control Release* 2018;**284**:188-212, https://doi.org/10.1016/j.jconrel.2018.06.026.

30. Vásquez Marcano RGDJ, Tominaga TT, Khalil NM, Pedroso LS, Mainardes RM. Chitosan functionalized poly (ε-caprolactone) nanoparticles for amphotericin B delivery. *Carbohydr Polym* 2018;**202**: 345-54, https://doi.org/10.1016/j.carbpol.2018.08.142.

31. Fernández-Álvarez F, García-García G, Arias JL. A tri-stimuli responsive (maghemite/PLGA)/chitosan nanostructure with promising applications in lung cancer. *Pharmaceutics* 2021;**13**:1232, https://doi.org/10.3390/pharmaceutics13081232.

32. Gao Y, Wu Y. Recent advances of chitosan-based nanoparticles for biomedical and biotechnological applications. *Int J Biol Macromol* 2022;**203**:379-88, https://doi.org/10.1016/j.ijbiomac.2022.01.162.

33. Massart R. Preparation of aqueous magnetic liquids in alkaline and acidic media. *IEEE T Magn* 1981;**17**:1247-8, https://doi.org/10.1109/tmag.1981.1061188.

34. El-Hammadi MM, Arias JL. Iron oxide-based multifunctional nanoparticulate systems for biomedical applications: a patent review (2008–present). *Expert Opin Ther Pat* 2015;**25**:691-709, https://doi.org/10.1517/13543776.2015.1028358.

35. Arias JL, Reddy LH, Couvreur P. Superior preclinical efficacy of gemcitabine developed as chitosan nanoparticulate system. *Biomacromolecules* 2011;**12**:97-104, https://doi.org/10.1021/bm101044h.

36. Lyon RJP. Infrared absorption spectroscopy. In: Zussman J, editor. *Physical Methods in Determinative Mineralogy*. London: Academic Press; 1967. p. 371-99.

37. Silverstein RM, Webster FX, eds. Spectrometric identification of organic compounds, 6th ed. New York: John Wiley & Sons.

38. Caro C, Gámez F, Quaresma P, Páez-Muñoz JM, Domínguez A, Pearson JR, et al. Fe$_3$O$_4$-Au core-shell nanoparticles as a multimodal platform for in vivo imaging and focused photothermal therapy. *Pharmaceutics* 2021;**13**:416, https://doi.org/10.3390/pharmaceutics13030416.

39. Daneshmand S, Golmohammadzadeh S, Jaafari MR, Movaffagh J, Rezaee M, Sahebkar A, et al. Encapsulation challenges, the substantial issue in solid lipid nanoparticles characterization. *J Cell Biochem* 2018; **119**:4251-64, https://doi.org/10.1002/jcb.26617.

40. Carissimi G, Montalbán MG, Víllora G, Barth A. Direct quantification of drug loading content in polymeric nanoparticles by infrared spectroscopy. *Pharmaceutics* 2020;**12**:912, https://doi.org/10.3390/pharmaceutics12100912.

41. Ko M, Quiñones-Hinojosa A, Rao R. Emerging links between endosomal pH and cancer. *Cancer Metastasis Rev* 2020;**39**:519-34, https://doi.org/10.1007/s10555-020-09870-1.

42. Caro C, Carmen Muñoz-Hernández M, Leal MP, García-Martín ML. In vivo pharmacokinetics of magnetic nanoparticles. *Methods Mol Biol* 2018;**1718**:409-19, https://doi.org/10.1007/978-1-4939-7531-0_24.

43. El-Hammadi MM, Arias JL. Recent advances in the surface functionalization of PLGA-based nanomedicines. *Nanomaterials (Basel)* 2022; **12**:354, https://doi.org/10.3390/nano12030354.

44. Tee JK, Yip LX, Tan ES, Santitewagun S, Prasath A, Ke PC, et al. Nanoparticles' interactions with vasculature in diseases. *Chem Soc Rev* 2019;**48**:5381-407, https://doi.org/10.1039/c9cs00309f.

45. Almessiere MA, Slimani Y, Guner S, Sertkol M, Demir Korkmaz A, Shirsath SE, et al. Sonochemical synthesis and physical properties of Co$_{0.3}$Ni$_{0.5}$Mn$_{0.2}$Eu$_x$Fe$_{2-x}$O$_4$ nano-spinel ferrites. *Ultrason Sonochem* 2019;**58**104654, https://doi.org/10.1016/j.ultsonch.2019.104654.

46. Toth GB, Varallyay CG, Horvath A, Bashir MR, Choyke PL, Daldrup-Link HE, et al. Current and potential imaging applications of ferumoxytol for magnetic resonance imaging. *Kidney Int* 2017;**92**:47-66, https://doi.org/10.1016/j.kint.2016.12.037.

47. Pandey A, Dhas N, Deshmukh P, Caro C, Patil P, García-Martín ML, et al. Heterogeneous surface architectured metal-organic frameworks for cancer therapy, imaging, and biosensing: a state-of-the-art review. *Coord Chem Rev* 2020;**409**213212, https://doi.org/10.1016/j.ccr.2020.213212.

48. International Organization for Standardization. *Biological evaluation of medical devices — part 5: tests for in vitro cytotoxicity (ISO 10993-5:2009)*; 2009.

49. Al-Mahrouki A, Giles A, Hashim A, Kim HC, El-Falou A, Rowe-Magnus D, et al. Microbubble-based enhancement of radiation effect: role of cell membrane ceramide metabolism. *PloS One* 2017; **12**e0181951, https://doi.org/10.1371/journal.pone.0181951.

50. Cattel L, Airoldi M, Delprino L, Passera R, Milla P, Pedani F. Pharmacokinetic evaluation of gemcitabine and 2′,2′-difluorodeoxycytidine-5′-triphosphate after prolonged infusion in patients affected by different solid tumors. *Ann Oncol* 2006;**17**:v142-7, https://doi.org/10.1093/annonc/mdj970.

51. Paroha S, Verma J, Dubey RD, Dewangan RP, Molugulu N, Bapat RA, et al. Recent advances and prospects in gemcitabine drug delivery systems. *Int J Pharm* 2021;**592**120043, https://doi.org/10.1016/j.ijpharm.2020.120043.

52. Cabeza L, Ortiz R, Prados J, Delgado ÁV, Martín-Villena MJ, Clares B, et al. Improved antitumor activity and reduced toxicity of doxorubicin encapsulated in poly(ε-caprolactone) nanoparticles in lung and breast cancer treatment: an in vitro and in vivo study. *Eur J Pharm Sci* 2017; **102**:24-34, https://doi.org/10.1016/j.ejps.2017.02.026.

53. Unciti-Broceta JD, Arias JL, Maceira J, Soriano M, Ortiz-González M, Hernández-Quero J, et al. Specific cell targeting therapy bypasses drug resistance mechanisms in African trypanosomiasis. *PLoS Pathog* 2015;**11**e1004942, https://doi.org/10.1371/journal.ppat.1004942.

54. Wu H, Wang S, Fang H, Zan X, Zhang J, Wan Y. Chitosan-poly-caprolactone copolymer microspheres for transforming growth factor-β1 delivery. *Colloids Surf B Biointerfaces* 2011;**82**:602-8, https://doi.org/10.1016/j.colsurfb.2010.10.024.

55. Mai BT, Fernandes S, Balakrishnan PB, Pellegrino T. Nanosystems based on magnetic nanoparticles and thermo- or pH-responsive polymers: an update and future perspectives. *Acc Chem Res* 2018;**51**:999-1013, https://doi.org/10.1021/acs.accounts.7b00549.

56. Choi CH, Zuckerman JE, Webster P, Davis ME. Targeting kidney mesangium by nanoparticles of defined size. *Proc Natl Acad Sci U S A* 2011;**108**:6656-61, https://doi.org/10.1073/pnas.1103573108.

57. Mohseni M, Connell JJ, Payne C, Patrick PS, Baker R, Yu Y, et al. Scalable magnet geometries enhance tumour targeting of magnetic nano-carriers. *Mater Des* 2020;**191**108610, https://doi.org/10.1016/j.matdes.2020.108610.

58. Nichols JW, Bae YH. EPR: evidence and fallacy. *J Control Release* 2014;**190**:451-64, https://doi.org/10.1016/j.jconrel.2014.03.057.

59. Caro C, Avasthi A, Paez-Muñoz JM, Pernia Leal M, García-Martín ML. Passive targeting of high-grade gliomas via the EPR effect: a closed path for metallic nanoparticles? *Biomater Sci* 2021;**9**:7984-95, https://doi.org/10.1039/d1bm01398j.

60. Yhee JY, Jeon S, Yoon HY, Shim MK, Ko H, Min J, et al. Effects of tumor microenvironments on targeted delivery of glycol chitosan nanoparticles. *J Control Release* 2017;**267**:223-31, https://doi.org/10.1016/j.jconrel.2017.09.015.